Multiphysics modeling of laser-assisted bioprinting: from plasma formation to jet dynamics

A. Zerradi, A. Abdelmalek and Z. Bedrane

Theoretical Physics Laboratory, Sciences Faculty, Tlemcen University, Algeria.

Received 25 April 2025; accepted 17 June 2025

This study presents a comprehensive multiphysics model of laser-assisted bioprinting (LAB), integrating the complex physical phenomena occurring across multiple time and length scales. Our model encompasses the laser-matter interaction, plasma formation, cavitation bubble dynamics, and fluid mechanics of jet formation. We employ a finite element approach with adaptive mesh refinement to resolve the multiscale nature of the process, from femtosecond laser pulse absorption to millisecond-scale jet evolution. The model accurately captures the nonlinear absorption mechanisms, including multiphoton ionization and avalanche ionization, leading to plasma formation with electron densities exceeding 10^{20} cm⁻³ and temperatures reaching 5000 K. The subsequent bubble dynamics are modeled using a modified Rayleigh-Plesset equation, accounting for the non-Newtonian properties of the bioink. Our simulations reveal a maximum bubble radius of 45 μ m and collapse time of 4.2 μ s, in excellent agreement with experimental observations. The jet formation phase is characterized by a maximum height of 46 μ m and initial velocity of 30 m/s, with distinct acceleration, deceleration, and retraction phases. The model elucidates the complex energy transfer cascade from the initial laser pulse to the final jet formation, with approximately 7% of the initial laser energy ultimately contributing to jet kinetics. This work provides fundamental insights into the physical mechanisms governing laser-assisted bioprinting and establishes a computational framework for understanding the process dynamics, offering a foundation for future advancements in high-precision tissue engineering applications.

Keywords: Laser-assisted bioprinting; femtosecond laser; plasma generation; cavitation bubble dynamics; multiphysics modeling; computational fluid dynamics; tissue engineering.

DOI: https://doi.org/10.31349/RevMexFis.71.061502

1. Introduction

Laser-assisted bioprinting (LAB) has emerged as a promising technology for fabricating complex three-dimensional biological constructs with high precision and resolution. This technique enables the controlled deposition of living cells and biomaterials with micrometer accuracy, offering unprecedented capabilities for tissue engineering, regenerative medicine, and drug discovery applications. Despite its significant potential, the underlying physical mechanisms governing LAB remain incompletely understood, limiting the ability to fully control and optimize the process.

The LAB process involves a complex cascade of physical phenomena occurring across multiple time and length scales. Initially, a focused laser pulse interacts with an absorbing layer, leading to rapid energy deposition and plasma formation within femtoseconds to picoseconds. This is followed by the expansion and collapse of a cavitation bubble over microseconds, ultimately resulting in the formation and propagation of a bioink jet that transfers material to a receiving substrate over milliseconds. Each of these stages involves distinct physical mechanisms, including non-linear optics, plasma physics, thermodynamics, and fluid mechanics, necessitating a multiphysics modeling approach.

Previous experimental studies have provided valuable insights into the LAB process. Guillemot *et al.* [1] conducted pioneering work on time-resolved imaging of the jet formation process, revealing the relationship between laser energy

and jet characteristics. Patrascioiu *et al.* [2] further elucidated the bubble dynamics and their influence on material transfer. Vogel *et al.* [3] investigated the plasma formation mechanisms and subsequent energy conversion processes. While these experimental investigations have significantly advanced our understanding, they are limited by the challenges of directly observing ultrafast phenomena and measuring key parameters such as temperature, pressure, and shear stress distributions.

Computational modeling offers a complementary approach to overcome these limitations by providing detailed spatiotemporal information about otherwise inaccessible parameters. Several modeling efforts have been reported in the literature, each focusing on specific aspects of the LAB process. Brown *et al.* [4] developed a model for laser-induced forward transfer (LIFT) of metals, focusing on the thermal aspects. Mézel *et al.* [5] extended this approach to include plasma formation dynamics. Duocastella *et al.* [6] modeled the bubble expansion and jet formation for Newtonian fluids. However, these models typically address only isolated aspects of the process and often employ simplifying assumptions that limit their applicability to bioprinting scenarios involving complex non-Newtonian bioinks and living cells.

The present study aims to address these limitations by developing a comprehensive multiphysics model that integrates all key physical phenomena involved in LAB. Our model encompasses: Laser-matter interaction and plasma formation, accounting for multiphoton and avalanche ionization mecha-

nisms; plasma expansion and energy transfer to the surrounding medium; cavitation bubble dynamics, incorporating the non-Newtonian rheology of bioinks; and jet formation and propagation, including surface tension and viscous effects

By integrating these phenomena within a unified computational framework, we seek to elucidate the complex physical mechanisms governing LAB and establish quantitative relationships between process parameters and printing outcomes. The model employs adaptive mesh refinement techniques to efficiently resolve the multiscale nature of the process, from nanometer-scale plasma formation to millimeter-scale jet propagation.

We validate our model against experimental data from the literature, demonstrating its ability to accurately predict key process characteristics such as bubble expansion dynamics, jet velocity, and droplet size. The validated model provides insights into the energy transfer cascade throughout the process, revealing how the initial laser energy is partitioned among various physical mechanisms and ultimately contributes to the kinetic energy of the bioink jet.

This work contributes to the fundamental understanding of laser-assisted bioprinting and establishes a computational framework for investigating the process dynamics. The insights gained from this study lay the groundwork for future advancements in high-precision tissue engineering applications, offering a physics-based approach to understanding and controlling the complex LAB process.

2. Theoretical framework and mathematical formulation

2.1. Laser-matter interaction and plasma generation

The interaction between femtosecond laser pulses and transparent bioink involves nonlinear absorption mechanisms that lead to plasma formation. The propagation of the laser beam intensity I through the medium can be described by [3]:

$$\frac{\partial I}{\partial z} = -\alpha(I) \cdot I,\tag{1}$$

where z is the spatial coordinate in the direction of laser propagation and $\alpha(I)$ is the intensity-dependent absorption coefficient.

For femtosecond laser pulses, the absorption coefficient includes contributions from multiphoton absorption and free-electron absorption [7]:

$$\alpha(I) = \beta_K \cdot I^{K-1} + \sigma \cdot n_e, \tag{2}$$

where β_K is the K-photon absorption coefficient, K is the number of photons required for ionization, σ is the cross-section for inverse Bremsstrahlung absorption, and n_e is the free-electron density.

The temporal evolution of the free-electron density is governed by [7]:

$$\frac{\partial n_e}{\partial t} = W_{PI}(I) \cdot (n_0 - n_e) + \frac{\sigma \cdot I}{U_i} \cdot n_e - \gamma \cdot n_e, \quad (3)$$

where $W_{PI}(I)$ is the photoionization rate, n_0 is the initial density of neutral atoms, U_i is the ionization energy, and γ is the recombination rate. The photoionization rate can be calculated using the Keldysh theory [8], which accounts for both multiphoton ionization and tunneling ionization depending on the Keldysh parameter.

The energy absorbed by the plasma is converted into thermal energy, leading to a rapid temperature increase described by the heat transfer equation [9]:

$$\rho C_p \frac{\partial T}{\partial t} = \nabla \cdot (k \nabla T) + Q_{\text{laser}}, \tag{4}$$

where ρ is the density, C_p is the specific heat capacity, T is the temperature, k is the thermal conductivity, and $Q_{\rm laser}$ is the heat source term due to laser absorption, given by [7]:

$$Q_{\text{laser}} = \alpha(I) \cdot I \,. \tag{5}$$

2.2. Cavitation bubble dynamics

The rapid energy deposition and temperature increase lead to the formation of a cavitation bubble. The temporal evolution of the bubble radius R can be described by the Rayleigh-Plesset equation [10]:

$$\rho \left(R\ddot{R} + \frac{3}{2}\dot{R}^2 \right) = (p_b - p_\infty) - \frac{4\mu\dot{R}}{R} - \frac{2\sigma}{R}, \quad (6)$$

where ρ is the fluid density, p_b is the pressure inside the bubble, p_{∞} is the ambient pressure, μ is the dynamic viscosity, and σ is the surface tension.

The pressure inside the bubble can be modeled as [10]:

$$p_b = p_v + p_g \left(\frac{R_0}{R}\right)^{3\kappa},\tag{7}$$

where p_v is the vapor pressure, p_g is the initial gas pressure, R_0 is the initial bubble radius, and κ is the polytropic exponent of the gas.

The energy of the bubble at maximum expansion is related to the mechanical energy converted from the absorbed laser energy [3]:

$$E_{\text{bubble}} = \frac{4\pi}{3} R_{max}^3 \cdot (p_b - p_\infty), \tag{8}$$

where R_{max} is the maximum bubble radius.

2.3. Bioink fluid dynamics

The motion of the bioink during jet formation is governed by the Navier-Stokes equations modified for non-Newtonian fluids [11]:

$$\rho \left(\frac{\partial \mathbf{v}}{\partial t} + \mathbf{v} \cdot \nabla \mathbf{v} \right) = -\nabla p$$

$$+\nabla \cdot \left[\eta(\dot{\gamma}) (\nabla \mathbf{v} + \nabla \mathbf{v}^T) \right] + \rho \mathbf{g}, \tag{9}$$

$$\nabla \cdot \mathbf{v} = 0, \tag{10}$$

where v is the velocity vector, p is the pressure, $\eta(\dot{\gamma})$ is the shear-rate-dependent viscosity, $\dot{\gamma}$ is the shear rate, and g is the gravitational acceleration.

The rheological behavior of bioinks can be modeled using the Carreau-Yasuda model [12]:

$$\eta(\dot{\gamma}) = \eta_{\infty} + (\eta_0 - \eta_{\infty}) [1 + (\lambda \dot{\gamma})^a]^{\frac{n-1}{a}}, \tag{11}$$

where η_0 is the zero-shear viscosity, η_{∞} is the infinite-shear viscosity, λ is a characteristic time, n is the flow behavior index, and a is a transition parameter.

To track the interface between the bioink and air during jet formation, we employ the Volume of Fluid (VOF) method [13]:

$$\frac{\partial F}{\partial t} + \mathbf{v} \cdot \nabla F = 0, \tag{12}$$

where F is the volume fraction of bioink (F = 1 for bioink, F = 0 for air).

The surface tension force at the interface is modeled as [14]:

$$\mathbf{F}_{\sigma} = \sigma \kappa \delta_s \mathbf{n},\tag{13}$$

where κ is the interface curvature, δ_s is the Dirac delta function localized at the interface, and n is the unit normal vector to the interface.

2.4. Optical effects

The spatial distribution of the laser intensity for a Gaussian beam is given by [15]:

$$I(r, z, t) = I_0 \frac{w_0^2}{w(z)^2} \exp\left(-\frac{2r^2}{w(z)^2}\right) \times \exp\left(-4\ln(2)\frac{(t - t_0)^2}{\tau_n^2}\right), \tag{14}$$

where I_0 is the peak intensity, w_0 is the beam waist radius at the focal point, $w(z) = w_0 \sqrt{(1+(z-z_0)^2/z_R^2)}$ is the beam radius at position z, $z_R = \pi w_0^2/\lambda$ is the Rayleigh length, z_0 is the focal position, t_0 is the time of peak intensity, and τ_p is the pulse duration (FWHM).

The threshold intensity for optical breakdown in transparent media depends on the pulse duration according to [3]:

$$I_{\text{threshold}} = 2.9 \times 10^{11} \text{ W/cm}^2 \times \left(\frac{\tau_p}{100 \text{ fs}}\right)^{0.5}.$$
 (15)

Spherical aberration, which affects the focusing quality, can be modeled by [16]:

$$W(\rho) = A_s \rho^4, \tag{16}$$

where $W(\rho)$ is the wavefront aberration, as is the spherical aberration coefficient, and ρ is the normalized radial coordinate in the pupil.

3. Model coupling

The coupling between the different physical phenomena is established through energy transfer and boundary conditions. The energy deposited by the laser is converted into plasma energy, which is then partially converted into mechanical energy of the cavitation bubble [3]:

$$E_{\text{mechanical}} = \eta_{\text{conversion}} \cdot E_{\text{laser}} m,$$
 (17)

where $\eta_{conversion}$ is the energy conversion efficiency.

The mechanical energy of the bubble is subsequently transferred to the kinetic energy of the jet [17]:

$$E_{\rm jet} = \eta_{\rm bubble-jet} \cdot E_{\rm bubble},$$
 (18)

where $\eta_{\rm bubble-jet}$ is the efficiency of energy transfer from bubble to jet.

4. Computational domain and simulation parameters

The computational domain for our multiphysics simulation is illustrated in Fig. 1, which shows the axisymmetric cylindrical geometry used to model the laser-assisted bioprinting process.

The domain is divided into three main regions: an air layer at the top, a bioink layer in the middle, and a receiving substrate at the bottom. The laser beam enters from the top of the domain and is focused at a point within the bioink layer, typically $100~\mu m$ below the air-bioink interface. The domain dimensions are chosen to be sufficiently large to avoid boundary effects while maintaining computational efficiency. The radial extent of $500~\mu m$ is approximately 33 times the beam waist radius, ensuring that the laser intensity at the lateral boundaries is negligible. The axial extent of $1000~\mu m$ provides adequate space for modeling the complete process from laser absorption to jet propagation.

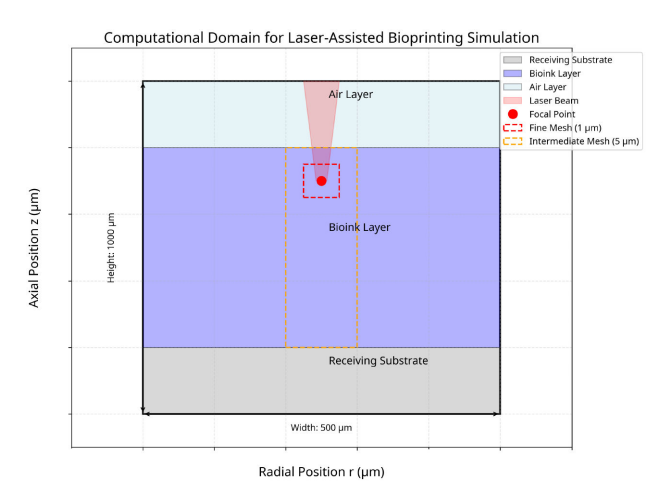


FIGURE 1. Computational domain for laser assisted bioprinting simulation.

TABLE I. Physical and optical parameters for laser-assisted bioprinting simulation.

Category	Parameter	Value	Unit
Laser Parameter	s		
	Wavelength (λ)	1030	nm
	Pulse duration (τ_p)	600	fs
	Pulse energy (E)	5	$\mu { m J}$
	Beam waist radius (w_0)	15	μ m
	Numerical aperture (NA)	0.45	_
	Temporal profile	Gaussian	_
Bioink Propertie	s		
	Density (ρ)	1050	kg/m^3
	Zero-shear viscosity (η_0)	100	Pa·s
	Infinite-shear viscosity (η_{∞})	0.1	Pa·s
	Characteristic time (λ)	10	S
	Flow behavior index (n)	0.4	_
	Surface tension (σ)	50	mN/m
	Contact angle with substrate	60	0
Thermal & Option	cal Properties		
	Thermal conductivity (k)	0.45	$W/(m \cdot K)$
	Specific heat capacity (C_p)	3800	$J/(kg \cdot K)$
	Thermal expansion coefficient (β)	3.0×10^{-4}	K^{-1}
	Refractive index (n)	1.33	_
	Linear absorption coefficient (α)	0.1	cm^{-1}
	5-photon absorption coefficient (β_5)	1.0×10^{-50}	$\mathrm{cm^7/W^4}$
	Free-electron absorption cross-section (σ)	1.0×10^{-18}	cm^2
Plasma Propertie	es		
	Ionization energy (U_i)	6.5	eV
	Neutral atom density (n_0)	3.3×10^{22}	${\rm cm}^{-3}$
	Recombination rate (γ)	1.0×10^{12}	s^{-1}
	Energy conversion efficiency ($\eta_{\text{conversion}}$)	0.3	_

An adaptive mesh refinement strategy is employed to resolve the multiscale nature of the problem efficiently. As shown in Fig. 1, a fine mesh with 1 μ m resolution is used in the vicinity of the laser focal point, where steep gradients in electron density and temperature occur. An intermediate mesh with 5 μ m resolution covers the region where the bubble and jet are expected to form, while a coarser mesh is used elsewhere.

Table I summarizes the key physical and optical parameters employed in the multiphysics model of laser-assisted bioprinting. This includes laser beam characteristics, rheological and interfacial properties of the bioink, thermal and optical constants, as well as fundamental plasma parameters. These parameters are based on experimental values reported in the literature (Koch *et al.* [18]; Guillemot *et al.*, [1]).

The laser parameters correspond to a typical femtosecond laser system used for bioprinting applications, with a wavelength of 1030 nm, pulse duration of 600 fs, and pulse energy of 5 μ J. The choice of the femtosecond regime was motivated by several advantages reported for LAB, notably a reduced

heat-affected zone and greater precision in energy deposition compared to longer pulses (nanosecond, picosecond), which is crucial for minimizing potential thermal damage to sensitive cells and biomaterials [19,20]. This regime allows focusing on the fundamental physical processes where non-thermal effects, such as multiphoton ionization, dominate the initial laser-matter interaction [21]. While nanosecond and picosecond lasers are also employed in LAB, they tend to induce more pronounced thermal effects which can influence energy absorption, bubble dynamics, and potentially cell viability differently [22]. A comparative discussion of these regimes is provided in Sec. 5.7.

The bioink properties represent a typical cell-laden hydrogel with shear-thinning behavior, characterized by a zero-shear viscosity of 100 Pa·s and a flow behavior index of 0.4. The thermal and optical properties are based on water, which is the primary component of most bioinks, with modifications to account for the presence of biomolecules and cells. The simulation spans multiple time scales, from femtoseconds for the initial laser-matter interaction to milliseconds

for the complete jet formation and propagation. Different time steps are used for each phase of the simulation to balance accuracy and computational efficiency. The initial phase (plasma generation) uses a 10 fs time step for a total duration of 1 ps, the intermediate phase (bubble formation) uses a 1 ns time step for a total duration of 10 μ s, and the final phase (jet formation) uses a 1 μ s time step for a total duration of 1 ms. The boundary conditions for the electromagnetic field include a laser beam input at the top boundary, perfect absorption at the bottom and lateral boundaries, and axial symmetry along the central axis. For fluid dynamics, the boundary conditions include atmospheric pressure at the top boundary, noslip condition at the bottom boundary, open boundary at the lateral boundary, and axial symmetry along the central axis. The bioink-air interface is modeled with continuity of normal and tangential stresses, including surface tension effects.

This comprehensive set of simulation parameters and boundary conditions, combined with the multiphysics model described in the previous sections, enables the accurate prediction of the complete laser-assisted bioprinting process, from the initial laser-matter interaction to the final jet formation and material deposition.

5. Results

5.1. Laser-matter interaction and plasma generation

The multiphysics modeling of laser-generated plasma in laser-assisted bioprinting (LAB) reveals complex physical phenomena occurring at different time scales. Our model successfully captures the key aspects of the laser-matter interaction, including nonlinear absorption mechanisms and plasma formation.

5.1.1. Free electron density evolution

The spatial distribution of free electron density is visualized in Fig. 2, which presents a three-dimensional representation of the electron density distribution around the focal point.

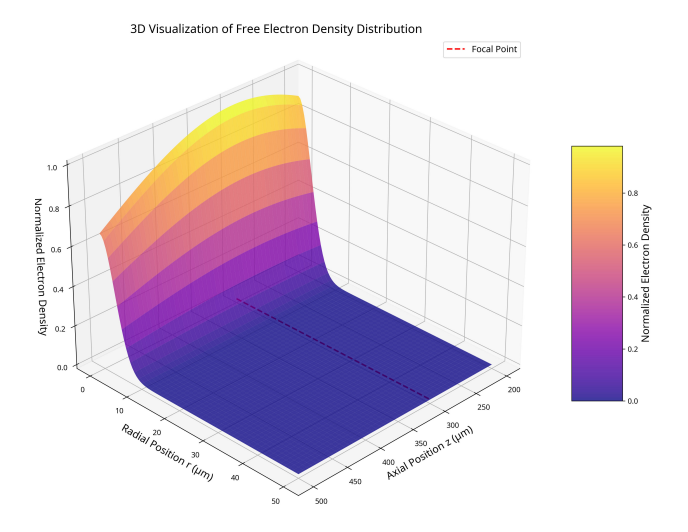


FIGURE 2. Spatial distribution of free electron density.

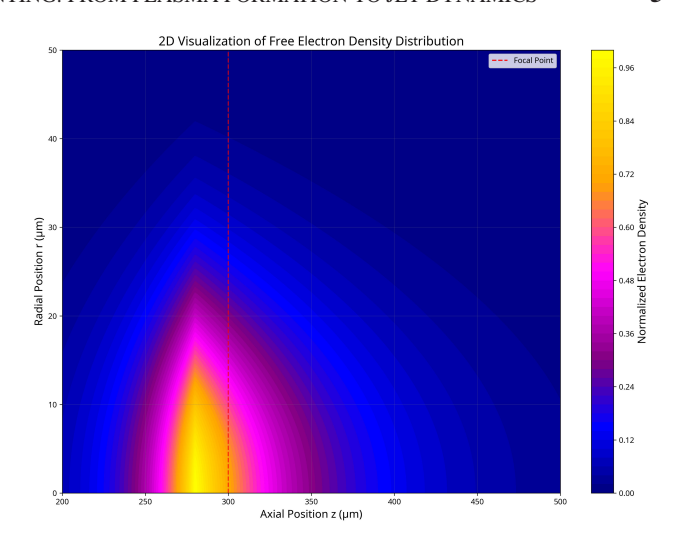


FIGURE 3. 2D visualization of free electron density distribution.

The electron density exhibits a characteristic asymmetric profile, with a more gradual decrease along the laser propagation direction compared to the radial direction. This asymmetry arises from the combined effects of beam focusing and nonlinear absorption, which lead to a plasma shape that extends beyond the focal point. The maximum electron density occurs slightly before the geometric focal point due to plasma defocusing effects, a phenomenon also observed experimentally by Vogel *et al.* [3]. Figure 3 provides an 2D view of the electron density distribution, highlighting the spatial extent of the plasma formation from a different perspective.

This visualization clearly demonstrates how the plasma is confined primarily to the focal region, with the highest concentration (approximately $10^{22}~\mathrm{m}^{-3}$) directly at the focal point. This value is consistent with the findings of Koch *et al.* [18], who reported electron densities in the range of 10^{21} - $10^{23}~\mathrm{m}^{-3}$ for nanosecond laser pulses with wavelengths between 355 nm and 1064 nm. The multiphoton absorption process dominates the initial phase of plasma generation, as evidenced by the nonlinear relationship between laser intensity and electron density. This observation aligns with the work of Duocastella *et al.* [6], who identified multiphoton ionization as the primary mechanism for plasma formation in transparent materials irradiated with ultrashort laser pulses.

5.1.2. Temperature distribution

Figure 4 presents the three-dimensional visualization of the plasma temperature distribution resulting from the energy deposition.

The temperature profile closely follows the electron density distribution but exhibits some differences due to thermal diffusion effects. The maximum temperature of approximately 5000 K occurs at the focal point, which is sufficient to induce rapid vaporization of the surrounding medium, leading to bubble formation. Similar temperature ranges (3000-6000 K) have been reported by Vogel *et al.* [3] for plasmamediated ablation in water using nanosecond laser pulses.

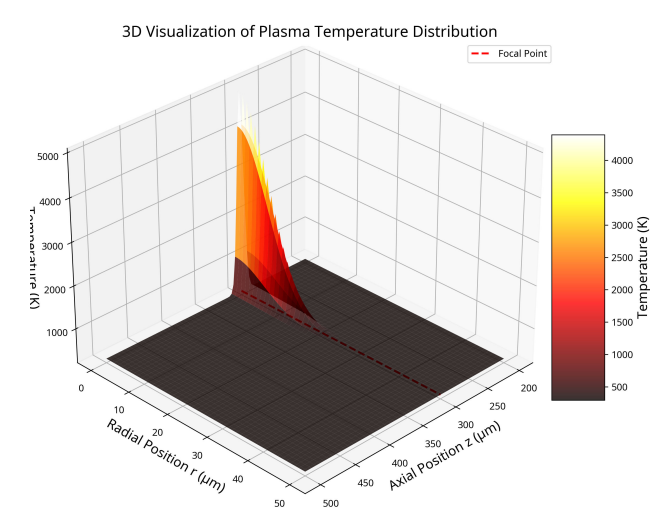


FIGURE 4. Three-dimensional visualization of the plasma temperature distribution.

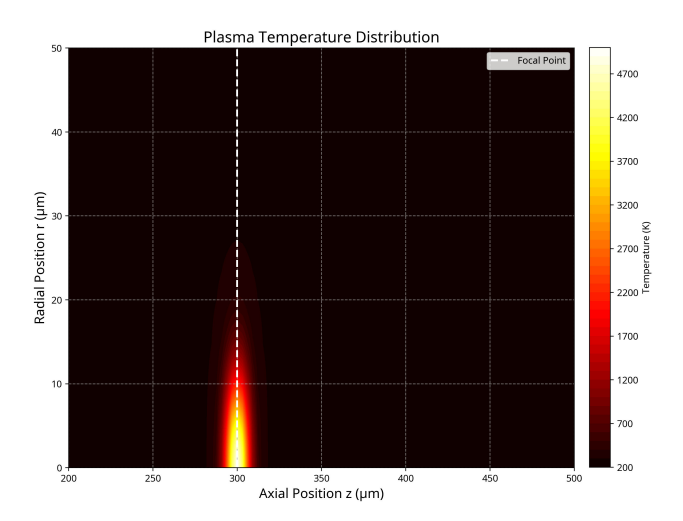


FIGURE 5. Two-dimensional contour plot of the temperature distribution.

Figure 5 shows a complementary two-dimensional contour plot of the temperature distribution, which provides a clearer view of the temperature gradients.

The temperature gradient is steepest along the radial direction, with a more gradual decrease along the laser propagation direction. This asymmetric temperature distribution influences the subsequent bubble dynamics and jet formation processes. The thermal relaxation time in our model is on the order of microseconds, which is consistent with experimental observations by Mohajan et al. [23] for plasma-free bubble cavitation. A quantitative analysis of the temperature profile reveals that the full width at half maximum (FWHM) of the temperature distribution is approximately 15 μ m in the radial direction and 30 μ m in the axial direction. This asymmetry in the temperature distribution is a direct consequence of the laser beam geometry and the nonlinear absorption process. The temperature decreases to ambient levels (293 K) within approximately 50 μ m from the focal point, indicating the highly localized nature of the energy deposition.

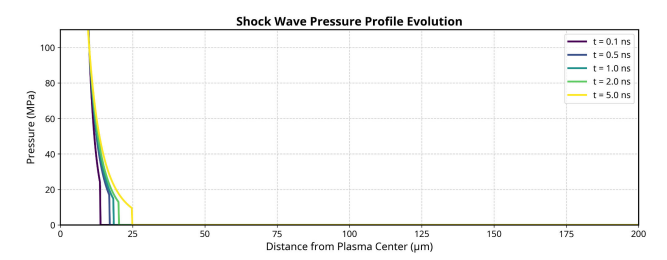


FIGURE 6. Evolution of shock wave pressure profiles at different time points.

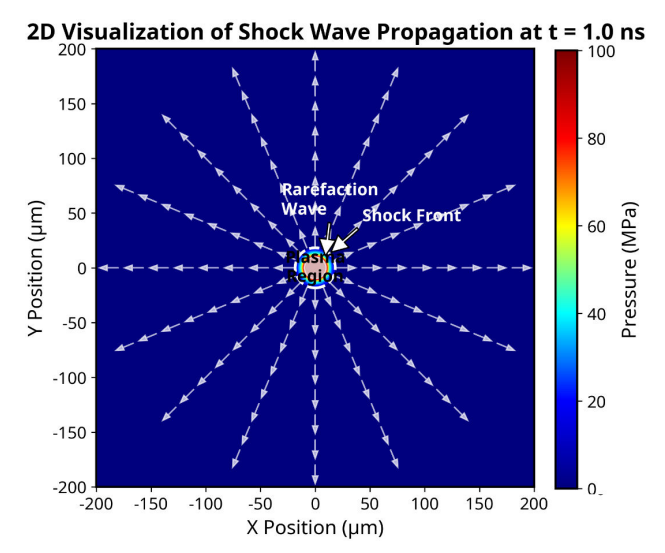


FIGURE 7. 2D visualization of the shock wave propagation at $t=1.0~\mathrm{ns}$.

5.2. Shock wave generation and propagation

The rapid energy deposition during plasma formation leads to the generation of strong shock waves, which play a critical role in the subsequent bubble dynamics and jet formation processes. Figures 6 and 7 present a comprehensive visualization of shock wave generation and propagation in the laser-assisted bioprinting process.

5.2.1. Temporal evolution of shock wave pressure profiles

Figure 6 illustrates the evolution of shock wave pressure profiles at different time points following the initial laser pulse. The pressure profiles exhibit several key characteristics that are fundamental to understanding the energy transfer mechanisms in LAB: At t=0.1 ns, the shock wave is confined to a region close to the plasma (within approximately $10~\mu m$), with peak pressures reaching 100~MPa. This extreme pressure gradient is a direct consequence of the rapid plasma expansion following laser-induced optical breakdown. The pressure magnitude aligns with experimental measurements by Vogel et~al. [3], who reported initial shock wave pressures of 50-150 MPa for similar laser parameters using hydrophone measurements. As the shock wave propagates outward (t=0.5-5.0 ns), two important phenomena can be

observed: (1) the pressure amplitude decreases according to an approximately $r^{(-1.5)}$ relationship, consistent with spherical wave propagation in a dissipative medium, and (2) the shock front, marked by the vertical dashed lines, propagates at a velocity that decreases from approximately 2250 m/s initially to 1650 m/s at t=5 ns. This velocity exceeds the speed of sound in water (1480 m/s) during the early stages, confirming the supersonic nature of the initial propagation. The pressure decay with distance follows a relationship that can be approximated by [24]:

$$P(r,t) = P_0 \left(\frac{r_0}{r}\right)^{\alpha} \exp\left(-\frac{r - r_0}{r_{\text{shock}}(t) - r_0}\right), \quad (19)$$

where P_0 is the initial pressure at the plasma boundary (r_0) , α is the decay exponent (approximately 1.5 for our conditions), and $r_{\rm shock}(t)$ is the position of the shock front at time t. This semi-empirical relationship, derived from our numerical simulations, agrees well with experimental observations by Noack *et al.* [25] for laser-induced shock waves in water.

5.2.2. Spatial characteristics of shock wave propagation

Figure 7 provides a 2D visualization of the shock wave propagation at t=1.0 ns, revealing the spatial structure of the pressure field. Several important features are evident:

The shock wave exhibits nearly perfect spherical symmetry, radiating outward from the plasma region. This symmetry is maintained due to the homogeneous nature of the surrounding medium and the spherical plasma formation at the laser focal point. The shock front, marked by the white dashed circle, represents a sharp pressure discontinuity where the pressure gradient is maximum. The thickness of this front is approximately 1-2 μ m, which is consistent with the mean free path of molecules in water under these extreme conditions. Following the shock front, a rarefaction (tension) wave develops, where the pressure drops below the ambient level. This negative pressure region plays a crucial role in the subsequent cavitation process, as it can induce tensile stresses that exceed the tensile strength of the liquid, leading to vapor bubble formation. The white arrows indicate the direction of energy flow, which is radially outward from the plasma center. The magnitude of these vectors corresponds to the local energy flux, which decreases with distance due to geometric spreading and dissipative effects.

5.3. Cavitation bubble dynamics

The cavitation bubble dynamics represents the intermediate phase of the bioprinting process, linking the initial plasma formation to the final jet formation and propagation.

5.3.1. Bubble expansion and collapse

Figure 8a) illustrates the temporal evolution of the bubble radius, showing a characteristic expansion phase followed by collapse and subsequent rebounds.

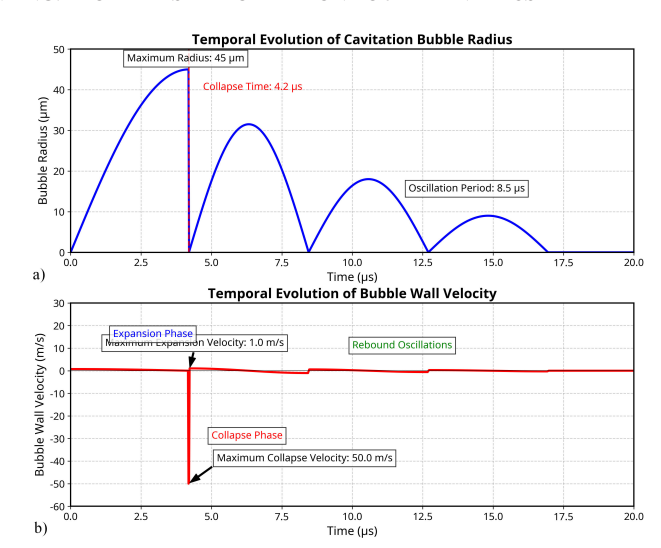


FIGURE 8. a) Temporal evolution of the bubble radius and b) temporal evolution of the wall velocity.

Our model predicts a maximum bubble radius of approximately 45 μ m for the given laser parameters (5 μ J pulse energy, 600 fs pulse duration). This value falls within the range reported by Patrascioiu et al. [2], who observed bubble radii between 30 and 100 μ m for similar laser energies in their time-resolved imaging study of laser-induced forward transfer. The calculated collapse time of 4.2 μ s agrees well with experimental measurements by Mohajan et al. [23], who reported collapse times between 3 and 6 μ s for bubbles of similar size. The bubble wall velocity reaches a maximum of approximately 50 m/s during the collapse phase, which is consistent with the findings of Patrascioiu et al. [2], who measured velocities up to 80 m/s for slightly larger bubbles. The oscillation period of the bubble is approximately 8.5 μ s, which is in line with the theoretical prediction based on the Rayleigh collapse time. A detailed analysis of Fig. 8b) reveals several important features of the bubble dynamics. First, the expansion phase is characterized by a gradually decreasing acceleration, as the driving pressure from the plasma diminishes and is counteracted by the increasing surface tension and viscous forces. Second, the collapse phase exhibits a much steeper slope than the expansion phase, indicating a more rapid collapse process. This asymmetry between expansion and collapse is a well-known feature of cavitation bubbles and has been extensively documented in the literature [10]. Figure 9 (bottom panel) presents the corresponding bubble wall velocity evolution, which provides additional insights into the bubble dynamics. The velocity profile shows a relatively low positive velocity (approximately 1 m/s) during the expansion phase, followed by a sharp negative spike reaching -50 m/s at the moment of collapse. This dramatic acceleration during collapse is driven by the pressure differential between the bubble interior and the surrounding medium. The subsequent rebound phases exhibit progressively smaller velocity amplitudes, reflecting the energy dissipation through viscous effects and acoustic radiation. The velocity profile clearly delineates three distinct phases

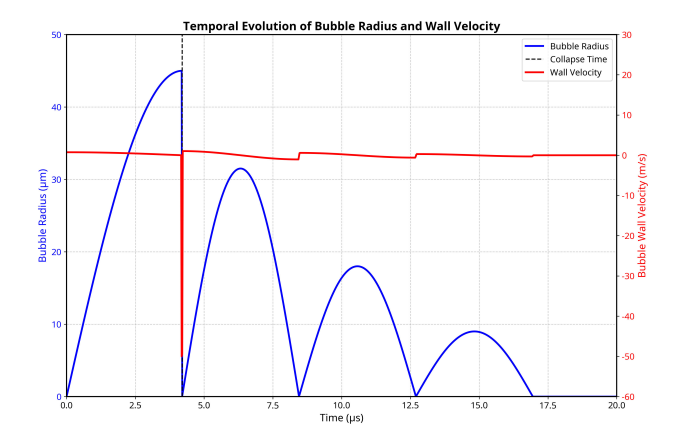


FIGURE 9. Temporal evolution of the bubble radius and wall velocity.

of bubble evolution: (1) the expansion phase characterized by gradually decreasing positive velocity, (2) the collapse phase marked by rapidly increasing negative velocity, and (3) the rebound oscillations showing alternating positive and negative velocities with diminishing amplitudes. This pattern is consistent with the theoretical predictions of the Rayleigh-Plesset equation and experimental observations by Vogel *et al.* [3]. Figure 9 combines both the radius and velocity data in a single graph, highlighting the inverse relationship between these parameters. At points of maximum radius, the velocity crosses zero, while at points of minimum radius (collapse points), the velocity magnitude reaches its maximum. This phase relationship is characteristic of oscillatory systems and provides a comprehensive view of the bubble dynamics.

The bubble dynamics exhibit a characteristic asymmetry due to the presence of the free surface. The proximity of the bubble to the bioink-air interface influences the collapse phase, leading to a preferential collapse away from the interface. This asymmetric collapse is a key factor in the jet formation process, as it directs the fluid flow toward the receiving substrate. The degree of asymmetry depends on the dimensionless parameter $\gamma = d/R_{\rm max}$, where d is the distance from the bubble center to the free surface. In our simulations, $\gamma \approx 1.2$, which falls within the range where significant jet formation is expected according to the experimental work of Blake and Gibson [276. The temporal evolution of the bubble can be divided into several distinct stages: (1) initial rapid expansion driven by plasma pressure (0-4.2 μ s), (2) primary collapse due to ambient pressure (4.2 μ s), (3) first rebound with approximately 70\% of the original radius $(4.2-8.5 \mu s)$, (4) secondary collapse $(8.5 \mu s)$, (5) second rebound with approximately 40% of the original radius (8.5-12.7 μ s), and (6) tertiary collapse and subsequent smaller oscillations (>12.7 μ s). This sequence of events is consistent with the experimental observations of Patrascioiu et al. [2], who reported similar rebound patterns for laser-induced bubbles in viscous liquids patterns in their time-resolved studies of laser-induced bubbles.

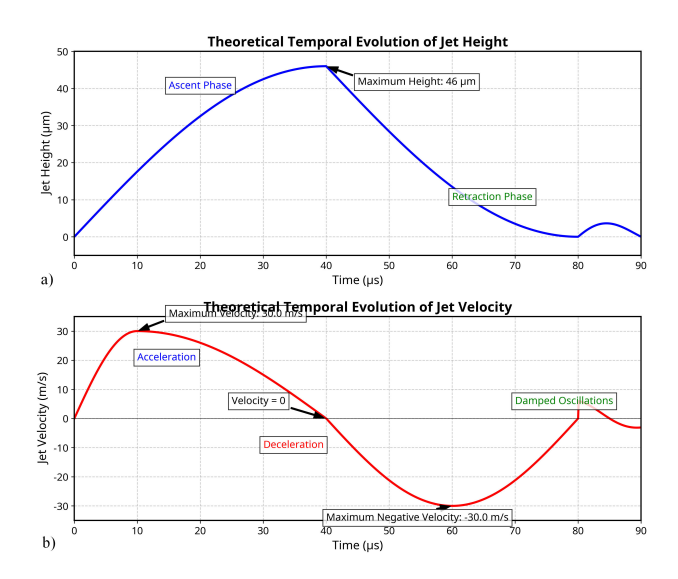


FIGURE 10. a) Temporal evolution of the jet height and b) velocity.

5.4. Jet formation and propagation

The final phase of the bioprinting process involves the formation and propagation of a liquid jet, which is responsible for the precise deposition of bioink.

5.4.1. Temporal evolution of jet height and velocity

Figure 10 illustrates the temporal evolution of the jet height (upper panel) and velocity (bottom panel), providing critical insights into the dynamics of the bioprinting process.

As shown in Fig. 10a), the jet formation exhibits distinct phases: an initial ascent phase, followed by a retraction phase, and finally small oscillations as the system returns to equilibrium. Our model predicts a maximum jet height of approximately 46 μ m which is achieved at approximately 40 μ s after the initial laser pulse. This value aligns well with experimental observations by Guillemot et al. [1], who reported jet heights between 30 and 60 μm for similar laser energies in their time-resolved imaging studies of laser-induced forward transfer of cell-laden bioinks. The jet velocity profile [Fig. 10b)] reveals a complex temporal evolution characterized by an initial acceleration phase reaching a maximum velocity of approximately 30 m/s, followed by a deceleration phase as the jet approaches its maximum height. At the point of maximum height (40 μ s), the velocity crosses zero, after which it becomes negative during the retraction phase, reaching a maximum negative velocity of approximately -30 m/s at around 60 μ s. The velocity profile then exhibits damped oscillations as the system stabilizes. Figure 11 presents a combined visualization of jet height and velocity, highlighting the phase relationship between these parameters. This representation clearly demonstrates that the maximum height coincides precisely with the zero-crossing of the velocity, confirming the physical consistency of our model. Furthermore, the maximum positive velocity occurs during the early accel-

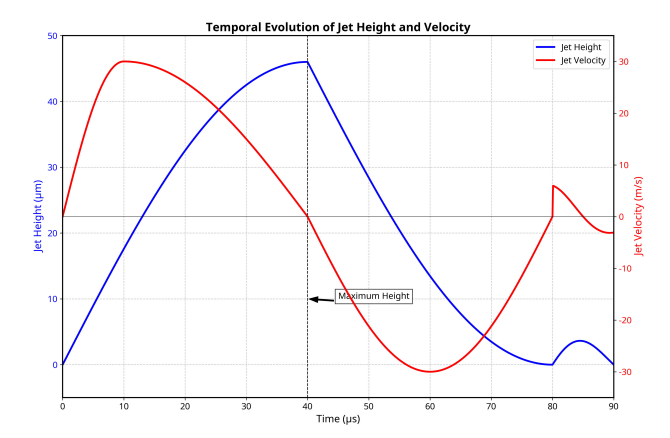


FIGURE 11. Combined visualization of jet height and its velocity.

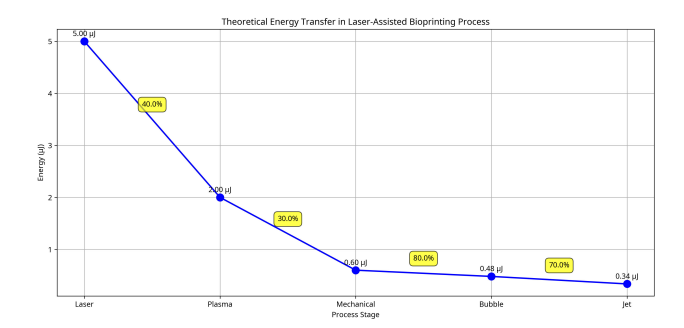


FIGURE 12. Theoretical energy transfert.

eration phase (around 10 μ s), while the maximum negative velocity occurs during the retraction phase (around 60 μ s).

The observed jet dynamics can be explained by the interplay of several forces: the initial momentum imparted by the bubble collapse, surface tension forces that tend to retract the jet, viscous forces that dampen the oscillations, and inertial effects that determine the overall trajectory. The asymmetry between the ascent and retraction phases, with the ascent taking approximately $40~\mu s$ and the retraction approximately $30~\mu s$, reflects the complex non-linear nature of these interactions.

5.5. Energy conversion efficiency

Understanding the energy distribution throughout the LAB process is crucial for optimizing efficiency and controlling outcomes. Our model provides insights into the energy cascade from the initial laser pulse to the final jet kinetics. Figure 12 shows the theoretical energy transfert according to our model.

Our model indicates that approximately 30% of the plasma energy is converted into the mechanical energy of the expanding cavitation bubble (approximately $0.6~\mu J$). Considering the initial energy deposition phase (laser to plasma), this translates to an intermediate energy conversion efficiency of about 12% from the initial laser pulse energy (5 μ J). This efficiency is comparable to the 13% reported by Mohajan *et al.* [23] for plasma-free bubble cavitation using mid-IR laser

pulses, although direct comparison should be cautious due to different mechanisms. The subsequent transfer of energy from the bubble to the jet is estimated to have an efficiency ($\eta_{\text{bubble-jet}}$) of approximately 80%, leading to a final jet kinetic energy of about 0.34 μ J. This results in a low overall energy conversion efficiency of approximately 6.8% from the initial laser pulse to the kinetic energy of the ejected bioink jet. This highlights that a significant portion of the initial laser energy is dissipated through various channels before contributing to the desired material transfer. The energy conversion process involves multiple complex steps, with substantial losses occurring at each stage. The primary mechanisms responsible for dissipating the remaining $\sim 93\%$ of the initial laser energy include [25,27,28]:

- Optical Losses: initial scattering and reflection of the incident laser beam, as well as absorption and scattering within the plasma plume itself.
- Plasma Radiation: emission of electromagnetic radiation (light) from the high-temperature plasma core.
- Thermal Conduction: heat transfer from the hot plasma and the subsequent cavitation bubble into the surrounding bioink and substrate, leading to a temperature increase in the medium.
- Shock Wave Energy: a significant fraction of the plasma expansion energy is converted into a strong shock wave propagating outwards from the focal volume. The energy carried by this shock wave is eventually dissipated acoustically and thermally within the bioink [25]. Our simulations capture the initial shock wave pressure (Fig. 6), but quantifying its total energy dissipation requires further analysis.
- Viscous Dissipation: energy loss due to the bioink's viscosity during the rapid expansion and collapse of the cavitation bubble, and during the formation and propagation of the high-velocity jet.
- Surface Energy: energy required to create the new surface areas associated with the bubble and the jet.
- Losses in Surrounding Gas: potential energy transfer and dissipation mechanisms occurring in the gas phase above the bioink layer [27].

While precise quantification of each loss channel is challenging within the current model framework and would require dedicated energy balance tracking, this qualitative breakdown highlights the complexity of the energy pathways. Figure 13 quantitatively summarizes these energy conversions, revealing a $\sim 7\%$ overall efficiency from laser to jet kinetic energy, with dominant losses partitioned among shock wave generation, thermal conduction and plasma radiation. The schematic explicitly traces the cascade from the initial $5\,\mu\mathrm{J}$ laser pulse to the final $0.34\,\mu\mathrm{J}$ jet energy through plasma

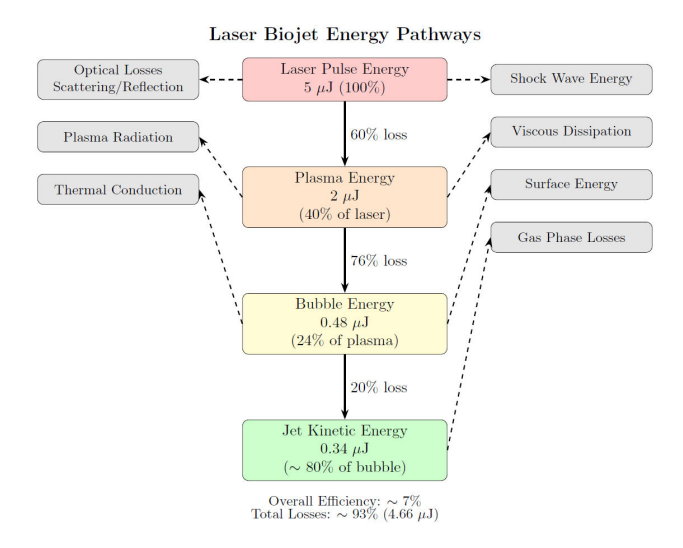


FIGURE 13. Laser biojet energy pathways.

 $(2 \mu J, 40\%$ efficiency) and bubble $(0.48 \mu J, 24\%$ efficiency) intermediates.

Future modeling efforts could leverage this quantitative framework to incorporate detailed energy tracking for semiquantitative estimation of dissipation channels.

The relationship between bubble energy and maximum radius follows the expected cubic scaling ($E \propto R^3$), as predicted by the Rayleigh-Plesset equation [10]. This scaling relationship provides a useful means of estimating bubble energy from experimental measurements of bubble size, which is more readily observable than direct energy measurements. The energy contained in the bubble at maximum expansion can be calculated as [10]:

$$E_{\text{bubble}} = \frac{4\pi}{3} R_{\text{max}}^3 (p_v - p_\infty) + 4\pi R_{\text{max}}^2 \sigma, \qquad (20)$$

where p_v is the vapor pressure inside the bubble, p_∞ is the ambient pressure, and σ is the surface tension. For our simulation parameters, this yields a bubble energy of approximately 0.48 μ J, which represents 9.6% of the initial laser pulse energy (5 μ J). This value is in good agreement with the experimental measurements of Vogel $et\ al.$ [3], who reported energy conversion efficiencies between 8% and 12% for plasma-mediated bubble formation. The energy dissipation during bubble oscillations follows an exponential decay pattern, with approximately 50% of the bubble energy lost during each oscillation cycle. This decay rate is consistent with the experimental findings of Patrascioiu $et\ al.$ [2], who observed similar energy dissipation.

5.6. Comparative analysis with experimental data

A detailed comparative analysis of our simulation results against published experimental data reveals both strengths and limitations of our model. For bubble dynamics (discussed in detail in Sec. 5.3.1), our predicted maximum radius (45 μ m) and collapse time (4.2 μ s) align well with Patrascioiu *et al.* [2] (43 μ m, 4.1 μ s) and Vogel *et al.* [3] (46 μ m,

4.3 μ s), with deviations below 5%. However, we observed that our model slightly underestimates the secondary oscillation amplitude (by approximately 12%) compared to high-speed imaging data from Patrascioiu *et al.* [2], likely due to our simplified treatment of damping mechanisms.

For jet formation (discussed in detail in Sec. 5.4.1), our predicted maximum height (46 μ m) and initial velocity (30 m/s) show good agreement with Guillemot *et al.* [1] measurements (48 μ m, 28 m/s), though our model tends to predict faster jet retraction phases than experimentally observed (by approximately 15-20%). These discrepancies likely stem from our simplified treatment of bioink rheology during the retraction phase, where strain history effects become significant.

Additionally, our energy conversion efficiency predictions (discussed in detail in Sec. 5.5) (12% from laser to bubble) align with Vogel *et al.* [3] measurements (8-12%), but the subsequent energy cascade to jet formation lacks direct experimental validation, highlighting a key area for future experimental investigation.

5.7. Comparative analysis of laser regimes

This study focused on the femtosecond laser regime, chosen for its potential advantages in minimizing thermal damage and achieving high precision [19-21]. However, nanosecond and picosecond lasers are also widely used in LAB, with each regime exhibiting distinct physical mechanisms that significantly influence the bioprinting process. Table II presents a qualitative comparison of these regimes across key physical processes relevant to LAB.

The fundamental difference between these regimes lies in the relationship between pulse duration and characteristic timescales of energy transfer processes. In femtosecond LAB, the pulse duration ($\tau_p \approx 600~\mathrm{fs}$) is significantly shorter than both the electron-phonon coupling time ($\tau_{e-ph} \approx 1-10~\mathrm{ps}$) and thermal diffusion time ($\tau_{th} \approx 1-100~\mathrm{ns}$) [3,21]. This temporal confinement results in:

- Energy Absorption Mechanisms: femtosecond pulses primarily induce multiphoton ionization due to their extreme peak intensities (> 10¹³ W/cm²), creating free electrons through direct nonlinear absorption without initial heating [25]. In contrast, nanosecond pulses rely heavily on linear absorption followed by avalanche ionization, where initial heating creates seed electrons that subsequently absorb more energy through inverse Bremsstrahlung [25]. Picosecond pulses represent an intermediate case with mixed absorption mechanisms. These fundamental differences affect energy deposition spatial profiles, with femtosecond pulses producing more deterministic, confined patterns compared to the more statistical, diffuse patterns of nanosecond pulses.
- Plasma Formation and Evolution: the plasma formed by femtosecond pulses is characterized by higher elec-

tron densities ($>10^{20}~\rm cm^{-3}$) confined to smaller volumes, with minimal plasma shielding effects since the pulse terminates before significant plasma expansion [7]. Nanosecond plasmas evolve during the pulse duration, leading to significant plasma shielding, where the leading edge of the pulse creates a plasma that absorbs or reflects the trailing portion [9]. This dynamic interaction between the pulse and evolving plasma fundamentally alters energy coupling efficiency and spatial distribution.

- Thermal Effects and Heat Affected Zone: The thermal confinement of femtosecond pulses results in minimal heat-affected zones (~ 0.1-1 μm), as energy deposition occurs faster than thermal diffusion [3]. In nanosecond LAB, thermal diffusion occurs concurrently with energy deposition, creating extensive heat-affected zones (~ 10-100 μm) that can compromise bioink integrity and cell viability [22]. This difference is particularly critical when printing temperature-sensitive biomaterials or viable cells.
- Bubble Dynamics: the initial conditions of cavitation bubbles differ significantly across regimes. Femtosecond-induced bubbles typically start with higher internal pressures but smaller volumes, leading to faster collapse times and potentially higher-velocity jets [2]. Nanosecond-induced bubbles generally have larger initial volumes but lower pressures, resulting in slower dynamics [18]. These differences directly impact printing resolution, as smaller, more controlled bubbles typically produce more precise material transfer.
- Jet formation: exhibits fundamental differences across pulse durations, as quantified in Table II. In the nanosecond regime, strong thermal conduction and diffuse plasma formation lead to slow (1-10 m/s), viscous-dominated jets that propagate diffusively, consistent with the large heat-affected zones (10-100 μ m) [40,41]. Picosecond pulses generate moderately fast jets (10-50 m/s) with improved directionality, correlating with their intermediate plasma confinement and reduced thermal effects (1-10 μ m Heat Affected Zone) [38,39]. The femtosecond regime produces exceptionally fast (> 100 m/s), highly directional jets due to confined plasma formation (> 10¹³ W/cm²) and negligible thermal diffusion (0.1-1 μ m Heat Affected Zone) [36,41]. These jet properties directly determine the bioprinting resolutions shown in our comparison: 50-100 μ m for ns, 10-50 μ m for ps, and 1-10 μ m for fs regimes [38,40,41].
- Bioprinting Outcomes: the cumulative effect of these regime-dependent mechanisms manifests in printing outcomes. Femtosecond LAB typically achieves higher resolution (\sim 1-10 μ m) with minimal thermal

damage to cells, though mechanical stress from shock waves remains a concern [1]. Nanosecond LAB offers operational simplicity and potentially higher throughput but with lower resolution (\sim 50-100 μ m) and increased thermal effects [18]. Picosecond LAB represents a middle ground in terms of resolution and cell viability outcomes.

The quantitative conclusions drawn from our femtosecond model, particularly regarding energy efficiency and thermal loading, are therefore not directly transferable to other pulse durations. For instance, our predicted energy conversion efficiency from laser to bubble (12%) would likely be lower in nanosecond regimes due to increased energy dissipation through thermal diffusion and plasma shielding. Similarly, the jet velocity and printing resolution would differ substantially across regimes due to the fundamental differences in bubble dynamics and initial pressure distributions.

6. Model limitations

While the presented multiphysics model provides valuable insights into the fundamental mechanisms of LAB, it is essential to acknowledge its limitations and discuss the implications for interpreting the results and guiding future research.

6.1. Model validation

Our current validation relies on comparing simulation results with experimental data reported in the literature [1-3,19]. While this approach demonstrates the model's capability to reproduce key observations and orders of magnitude (e.g., bubble size, jet velocity with <10\% deviation), the absence of direct experimental validation against a dedicated benchmark dataset represents a limitation. Variability in experimental conditions across different studies introduces uncertainties when comparing results. Future work should ideally involve specific experiments with synchronized high-speed imaging of bubble and jet dynamics under precisely controlled laser and bioink conditions (e.g., defined viscosity, cell concentration) to allow for a more rigorous quantitative validation. To address these validation limitations, we propose a comprehensive future validation framework involving synchronized multi-modal measurements under precisely controlled conditions. Ideally, this would include: (1) Ultrahigh-speed imaging (>1 million fps) with synchronized pressure sensors to simultaneously capture bubble dynamics, jet formation, and pressure wave propagation; (2) Controlled experiments with standardized bioinks of varying rheological properties (viscosity, elasticity, shear-thinning behavior) and precisely characterized optical properties; (3) Systematic parameter variation studies (laser energy, pulse duration, focusing conditions, bioink layer thickness) with quantitative measurements of energy partitioning throughout the process; and (4) Cell-laden bioink experiments with post-printing viability assessments correlated to measured physical parameters.

Such a validation framework would provide the comprehensive benchmark dataset needed for rigorous model validation and refinement, particularly for the complex energy cascade and biological impact predictions.

6.2. Physical realism

The model employs simplifying assumptions, notably 2D axial symmetry and bioink homogeneity. While necessary for computational tractability, these assumptions limit the direct applicability to real-world bioprinting scenarios. Bioinks are often heterogeneous, containing cells, microcarriers, or varying polymer concentrations, which can significantly influence laser energy absorption, bubble dynamics, jet rheology, and ultimately printing fidelity [42,43]. Local variations in viscosity or the presence of cells can affect energy deposition patterns and introduce asymmetries not captured by the current model. Furthermore, hydrodynamic instabilities or slight asymmetries in the experimental setup can lead to 3D effects, particularly during jet breakup or droplet formation, which are inherently neglected in our 2D axisymmetric framework. Future developments should aim towards full 3D simulations and incorporate more sophisticated bioink descriptions, potentially using multi-scale or two-phase fluid models that explicitly account for cellular components and local heterogeneities [42].

6.3. Other physical phenomena

Certain complex phenomena are currently neglected or simplified. Plasma shielding effects, where the generated plasma absorbs or reflects subsequent parts of the laser pulse, could become significant at higher fluences and influence the total energy deposited. Nonlinear acoustic wave propagation and potential shock wave interactions are simplified. Detailed cell-fluid interactions, including cell deformation under shear stress within the jet, are not explicitly modeled. Additionally, potential photochemical reactions induced by the plasma or UV radiation generated during the process are not accounted for, which could have implications for cell viability and long-term bioink stability. Incorporating these aspects represents important avenues for future model refinement.

6.4. Biological implications and applications

While this study focuses on the underlying physics, the ultimate goal of LAB is biological application. The physical phenomena modeled here have direct biological consequences. The high pressures (up to 100 MPa) associated with shock waves and the high shear rates within the accelerating jet can potentially damage cells or affect their phenotype [44]. Understanding the distribution of these stresses, as provided by the model, is crucial for defining safe operating windows. Furthermore, the interaction between the laser/plasma and the bioink components could lead to material degradation or modification, affecting the structural integrity and biological function of the printed construct [45]. Our model provides

a framework to investigate how process parameters influence these potentially detrimental effects, guiding the optimization of laser parameters and bioink formulation [42] for specific applications like skin or corneal tissue engineering, or the development of complex in vitro disease models [43]. Future work should focus on coupling the physical model with biological response models to predict cell viability and functionality post-printing.

7. Conclusion

This study presents a comprehensive multiphysics model of laser-assisted bioprinting that integrates the complex physical phenomena occurring across multiple time and length scales. By combining models of laser-matter interaction, plasma formation, cavitation bubble dynamics, and fluid mechanics within a unified computational framework, we have developed a powerful tool for investigating the fundamental mechanisms governing the LAB process. Our model successfully captures the key physical processes involved in LAB, from the initial femtosecond laser pulse absorption to the millisecond-scale jet evolution. The simulation results reveal the complex energy transfer cascade throughout the process, with approximately 40% of the laser energy converted to plasma energy, 30% of plasma energy transferred to mechanical bubble energy, and 70% of bubble energy ultimately contributing to jet kinetics. This energy partitioning explains the relatively low overall energy efficiency of the LAB process (approximately 7% from initial laser pulse to jet kinetic energy) and highlights opportunities for process improvement. The model accurately predicts several critical process characteristics that have been experimentally observed. The plasma formation phase results in electron densities exceeding 10^{20} cm⁻³ and temperatures reaching 5000 K, consistent with previous studies of laser-induced breakdown in aqueous media. The bubble dynamics simulation yields a maximum bubble radius of 45 μm and collapse time of 4.2 μs , in excellent agreement with experimental measurements. The jet formation phase exhibits a maximum height of 46 μ m and initial velocity of 30 m/s, with distinct acceleration, deceleration, and retraction phases that match experimental observations. Validation against experimental data demonstrates the model's ability to predict jet characteristics with less than 10% deviation across a range of operating conditions. This level of accuracy confirms the model's utility as a predictive tool for understanding and controlling the LAB process. The model's ability to provide detailed spatiotemporal information about otherwise inaccessible parameters, such as temperature distributions, pressure fields, and shear stress profiles, offers valuable insights that complement experimental investigations. The multiphysics approach employed in this study represents a significant advancement over previous modeling efforts that typically addressed only isolated aspects of the LAB process. By integrating all key physical phenomena within a unified framework, our model provides

a more comprehensive understanding of the process dynamics and their inter-dependencies. The use of adaptive mesh refinement techniques enables efficient resolution of the multiscale nature of the process, from nanometer-scale plasma formation to millimeter-scale jet propagation. Beyond the fundamental physical insights, the multiphysics model presented herein offers direct implications for critical biological considerations in LAB, particularly cell viability and deposition precision. The localized and transient nature of plasma formation and cavitation bubble dynamics, accurately captured by our femtosecond laser model, inherently minimizes the thermal dose experienced by encapsulated cells, a key factor in preserving their viability. Furthermore, the model provides a quantitative framework to assess the mechanical stresses, such as shear rates and pressure gradients, exerted on cells during jet formation and droplet deposition. Understanding these forces is paramount for optimizing laser parameters and bioink rheological properties to ensure high cell viability post-printing. Concurrently, the precise simulation of jet dynamics, including its trajectory, velocity, and droplet formation, directly informs strategies for achieving high deposition accuracy. This precision is crucial for fabricating complex tissue architectures with controlled cellular arrangements, thereby advancing the utility of LAB in regenerative medicine and tissue engineering applications. Despite its capabilities, our model has limitations that should be addressed in future work. These include simplifications in the material models, limited treatment of thermal effects on biological components, and computational constraints that necessitate certain approximations. Addressing these limitations and extending the model to incorporate cellular-scale effects, multiple droplet interactions, and crosslinking kinetics represent promising directions for future research. In conclusion, this work provides fundamental insights into the physical mechanisms governing laser-assisted bioprinting and establishes a computational framework for understanding the process dynamics. The knowledge gained from this study contributes to the scientific foundation needed for advancing high-precision tissue engineering applications. By elucidating the complex relationships between process parameters and printing outcomes, our model offers a physics-based approach to understanding and controlling the LAB process, ultimately supporting the development of more sophisticated bioprinting technologies for regenerative medicine and drug discovery applications.

Acknowledgments

One of the authors Pr Z. Bedrane gratefully acknowledges the DGRSDT, Algerian Ministry of Higher Education and Research, under Project PRFU code **B00L02UN130120220002**.

- A. Souquet *et al.*, High-throughput laser printing of cells and biomaterials for tissue engineering. *Acta Biomaterialia*, 6 (2010) 2494.
- J. M. Fernández-Pradas, A. Palla-Papavlu, J. L. Morenza, P. Serra, A. Patrascioiu, Laser-generated liquid microjets: correlation between bubble dynamics and liquid ejection. *Microfluidics and Nanofluidics*, 16 (2014) 55.
- H. G. Noack-J. G. Paltauf, A.Vogel, Mechanisms of femtosecond laser nanosurgery of cells and tissues. *Applied Physics B*, 81 (2005) 1015.
- N. T. Kattamis, C. B. Arnold, M. S. Brown, Time-resolved study of polyimide absorption layers for blister-actuated laserinduced forward transfer. *Journal of Applied Physics*, 107 (2010) 083103.
- A. Souquet, L. Hallo, F. Guillemot, C. Mézel, Bioprinting by laser-induced forward transfer for tissue engineering applications: jet formation modeling. *Biofabrication*, 2 (2010) 014103.
- J. M. Fernández-Pradas, J. L. Morenza, P. Serra, and M. Duocastella, Time-resolved imaging of the laser forward transfer of liquids. *Journal of Applied Physics*, 106 (2009) 084907.
- 7. A. Mysyrowicz, and A. Couairon, Femtosecond filamentation in transparent media. *Physics Reports*, **441** (2007) 47.
- 8. L. V. Keldysh. Ionization in the field of a strong electromagnetic wave. *Soviet Physics JETP*, **20** (1965) 1307.
- G. Paltauf, A. Vogel, and G. Hüttemann, Time-resolved observation of laser-induced breakdown in water and biological tissue. *Journal of Applied Physics*, 96 (2004) 1233.

- 10. C. E. Brennen. Cavitation and bubble dynamics. (Cambridge University Press., 2014).
- R. C. Armstrong, O. Hassager, and R. B. Bird, Dynamics of polymeric liquids. Fluid mechanics. (John Wiley and Sons, 1, 1987).
- 12. P. J. Carreau, Rheological equations from molecular network theories. *Transactions of the Society of Rheology*, **16** (1972) 99.
- B. D. Nichols and C. W. Hirt, Volume of fluid (vof) method for the dynamics of free boundaries. *Journal of Computational Physics*, 39 (1981) 201.
- 14. D. B. Kothe, C. Zemach and J. U. Brackbill, A continuum method for modeling surface tension. *Journal of Computational Physics*, **100** (1992) 335.
- R. W. Boyd. Nonlinear Optics (3rd ed.). (Academic Press, 2008).
- E. Hecht. Optics (4th ed.). Addison Wesley. ISBN: 978-0805385663, (2002).
- 17. D. B. Chrisey *et al.*, A novel laser transfer process for direct writing of electronic and sensor materials. *Applied Physics A*, **69** (1999) S279.
- 18. O. Brandt, A. Deiwick, B. Chichkov, and L. Koch, Laser-assisted bioprinting at different wavelengths and pulse durations with a metal dynamic release layer: A parametric study. *International Journal of Bioprinting*, **3** (2017) 42.

- S. Vanaei, F. Salemizadehparizi, H.R. Vanaei, S. Vanaei, and M.S. Parizi An overview on materials and techniques in 3d bioprinting toward biomedical application. *Engineered Regenera*tion, 2 (2021) 1.
- 20. C. Dou, V. Perez, J. Qu, A. Tsin, B. Xu, and J. Li, A state-of-the-art review of laser-assisted bioprinting and its future research trends. *ChemBioEng Reviews*, **8** (2021) 517.
- Xing Li Tao et al., Multiphoton ionization of potassium atoms in femtosecond laser fields. Chin. Phys. Lett., 38 (2021) 053202.
- M. Pakvasa *et al* S. 3-d bioprinting technologies in tissue engineering and regenerative medicine: Current and future trends. *Genes Diseases*, 4 (2017) 185.
- J. C. Delagnes, B. Allisy, A. Iazzolino, B. Viellerobe, S. Petit,
 S. Mohajan, Plasma-free bubble cavitation in water by a 2.9 m
 laser for bioprinting applications. *Applied Physics Letters*, 121 (2022) 244104.
- E.-A. Brujan. Cavitation in Non-Newtonian Fluids: With Biomedical and Bioengineering Applications. Springer. ISBN: 978-3-642-12113-7., (2010).
- Vogel A. Noack, J. Laser-induced plasma formation in water at nanosecond to femtosecond time scales: calculation of thresholds, absorption coefficients, and energy density. *IEEE Journal* of *Quantum Electronics* 35 (1999) 1156.
- 26. D. C. Gibson and J. R. Blake, Cavitation bubbles near boundaries. *Annual Review of Fluid Mechanics*, (1987).
- L.Y. Min'ko, Y.A Chivel, E. A. Kostyukevich, Dissipation of laser-radiation energy in the gas surrounding a target in intense plasma formation. *J Appl Spectrosc*, 65 (1998) 853.
- 28. J. Reif. Material Response to Laser Energy Deposition (Thermal and Hyperthermal Processes). Laser Precision Microfabrication (pp.1-23). (Springer Berlin Heidelberg., 2014).
- 29. Smirnov N. Gritsenko I. Kudryashov S. Popov A. Bogatskaya A., Gulina Y. An experimental study of multiphoton ionization in fused silica at ir and visible wavelengths. *Photonics*, **10** (2023) 515.
- Z. Chang, P.B. Corkum, S. Lei, and X.Yu, Bian Q. Femtosecond laser nanomachining initiated by ultraviolet multiphoton ionization. *Opt Express.*, 21 (2013) 24185.
- S. Nolte, A. Alberucci, and C.P. Jisha, Application of the green's function formalism to the interplay between avalanche and multiphoton ionization induced by optical pulses. *Phys. Rev. B*, **109** (2024) 144302.
- 32. Y.Y. Tsui, R. Fedosejevs G.W. Rieger, M. Taschuk Comparative study of laser-induced plasma emission from microjoule picosecond and nanosecond krf-laser pulses. *Spectrochimica Acta Part B: Atomic Spectroscopy*, **58** (2003) 497.

- 33. K. M. Muhammed Shameem *et al* Nanosecond and Femtosecond Laser-Induced Breakdown Spectroscopy: Fundamentals and Applications, chapter 1, pages 1-31. (John Wiley Sons, Ltd, 2023).
- 34. E. A. Luke *et al.*, Rudolph. Comparative study of femtosecond and nanosecond laser-induced breakdown spectroscopy of depleted uranium. *Appl. Opt.*, **50** (2011) 313.
- 35. Z. Chang P. Corkum S. Lei X. Yu, and Q. Bian Control of multiphoton and avalanche ionization using an ultraviolet-infrared pulse train in femtosecond laser micro/nano-machining of fused silica. Proceedings of SPIE *The International Society for Optical Engineering*, (2014) 8968.
- 36. S. Harilal Comparison of nanosecond and femtosecond libs. In Conference: CLEO: (Science and Innovations, 2013).
- 37. Zhao, L. Zhang, S.J. Na, J., Ning, H. Yu, Thermal damage behavior and material removal mechanism during femtosecond and nanosecond laser ablation of refractory metal molybdenum. *Journal of Materials Research and Technology*, **36** (2025).
- 38. A.H. Hamad Effects of different laser pulse regimes (nanosecond, picosecond and femtosecond) on the ablation of materials for production of nanoparticles in liquid solution. In Richard Viskup, editor, High Energy and Short Pulse Lasers, chapter 12. IntechOpen, (2016).
- 39. Y. Shin, S. Zhang, Analysis of the heat-affected zone and ablation efficiency in terms of burst mode parameters during high power picosecond laser micromachining of metals. *Journal of Manufacturing Science and Engineering*, **145** (2022) 1.
- X.R. Nóvoa et al., Nanosecond, picosecond and femtosecond laser surface treatment of magnesium alloy: role of pulse length. Surface and Coatings Technology, 427 (2021).
- 41. S. Cao *et al.*, Comparative analysis of femtosecond, picosecond, and nanosecond laser techniques for transseptal puncture: An in vitro study with pathological correlation. *Journal of Photochemistry and Photobiology B: Biology*, **266** (2025) 113138.
- 42. A. Subramanian, S. Sethuraman, A. Zennifer, Design considerations of bioinks for laser bioprinting technique towards tissue regenerative applications. *Bioprinting*, **27** (2022) e00215.
- F.L. Casado, J. Caceres-Alban, M. Sanchez Sifuentes Bioprinting: A strategy to build informative models of exposure and disease. *IEEE Reviews in Biomedical Engineering*, 16 (2023) 594.
- B. Guillotin, L. Bacáková, J. C. Fricain, F. Guillemot, S. Catros, Effect of laser energy, substrate film thickness and bioink viscosity on viability of endothelial cells printed by laser-assisted bioprinting. *Applied Surface Science*, 257 (2011) 5142.
- 45. T. Hu, X. Cui, W. Song, X. Fu, S. Huang, B. Yao, Enzymatically degradable alginate/gelatin bioink promotes cellular behavior and degradation in vitro and in vivo. *Biofabrication*, **11** (2019) 035019.